Research Square

Preprints are preliminary reports that have not undergone peer review.
They should not be considered conclusive, used to inform clinical practice,
or referenced by the media as validated information.

A Hybrid Wavelet–Schur–HHL Framework for the Solution of Linear Elliptic and Hyperbolic Partial Differential Equations

J. B. Allen

jeffrey.b.allen@usace.army.mil

U.S. Army Engineer Research and Development Center

Research Article

Keywords: Multiresolution Analysis, Haar Wavelets, Schur Complement, Harrow–Hassidim–Lloyd Algorithm, Quantum Linear Systems, Quantum Computing

Posted Date: November 24th, 2026

DOI: https://doi.org/10.21203/rs.3.rs-11693279/v1

License: This work is licensed under a Creative Commons Attribution 4.0 International License.
Read Full License

Additional Declarations: No competing interests reported.

A Hybrid Wavelet–Schur–HHL Framework for the Solution of Linear Elliptic and Hyperbolic Partial Differential Equations

J.B. Allen

Information Technology Laboratory, U.S. Army Engineer Research and Development Center, Vicksburg, MS 39180, USA

Corresponding Author: Jeffrey.B.Allen@usace.army.mil

Abstract

This paper presents a hybrid Wavelet–Schur–Harrow–Hassidim–Lloyd (HHL) computational framework for the numerical solution of linear partial differential equations. The proposed methodology combines Haar wavelet-based multiresolution analysis with Schur complement reduction to construct compact sparse linear systems that are subsequently solved using the Harrow–Hassidim–Lloyd (HHL) quantum linear systems algorithm. Unlike conventional quantum PDE approaches that operate directly on finite-difference or finite-element discretizations, the present formulation applies quantum inversion to the Schur-reduced multiresolution system, thereby exploiting the hierarchical structure of the wavelet representation prior to the quantum solve. The methodology is validated using representative one- and two-dimensional elliptic and hyperbolic benchmark problems, including Poisson, oscillatory, exponential-source, Laplace, Helmholtz-type, advection, and wave equations. Across these benchmark problems, the hybrid HHL–Wavelet–Schur reconstructions remain in close agreement with the corresponding classical wavelet–Schur solutions, while the Schur reduction consistently produces smaller, better-conditioned linear systems for quantum solution. The results demonstrate that the proposed framework provides a unified approach for integrating quantum linear-system algorithms with multiresolution PDE discretizations across multiple classes of linear partial differential equations. All quantum computations were performed using noiseless statevector simulation, establishing a reproducible baseline for future implementations on fault-tolerant quantum hardware.

Keywords: Multiresolution Analysis; Haar Wavelets; Schur Complement; Harrow–Hassidim–Lloyd Algorithm; Quantum Linear Systems; Quantum Computing.

Mathematics Subject Classification (2020): 65N22 (Primary); 65T60, 68Q12, 65F10 (Secondary).

Funding

This research was supported by the U.S. Army Engineer Research and Development Center (ERDC) through the Military Engineering Basic Research Program.

1. Introduction

The numerical solution of large-scale partial differential equations (PDEs) remains one of the central challenges in computational science and engineering. As spatial discretizations become increasingly refined, the resulting sparse algebraic systems rapidly grow in size, motivating the development of multiscale numerical methods capable of reducing computational complexity while preserving solution accuracy. Among the most successful of these approaches is wavelet-based multiresolution analysis (MRA), which provides hierarchical representations capable of efficiently resolving localized solution features while naturally separating multiple spatial scales [1,2].

Multiresolution and hierarchical formulations originated in the pioneering work of Daubechies [3] and Mallat [4], whose developments established compactly supported orthogonal wavelets together with efficient multiresolution decomposition algorithms. Subsequent mathematical advances by Meyer [5] and Strang and Nguyen [6] extended these formulations into versatile numerical frameworks suitable for scientific computing. Wavelet-based MRA subsequently became an effective methodology for adaptive mesh refinement, sparse operator representations, and multiscale numerical simulation, with important contributions by Beylkin *et al.* [7] and the adaptive wavelet collocation methods developed by Vasilyev and Bowman [8].

Within computational mechanics and scientific computing, wavelet-based multiresolution methods have demonstrated the ability to substantially reduce computational expense while maintaining high numerical accuracy through hierarchical compression and adaptive resolution. Recent work has further demonstrated that Haar-based multiresolution analysis provides an efficient framework for the numerical solution of elliptic, parabolic, and hyperbolic partial differential equations through hierarchical basis representations and Schur-complement reduction, establishing a robust classical multiresolution framework upon which the present quantum formulation is built [9].

Although wavelet-based multiresolution methods significantly reduce computational complexity through hierarchical compression, the solution of the resulting sparse linear systems remains the dominant computational expense for sufficiently large problems. As discretizations become increasingly refined, classical iterative and direct solvers continue to exhibit polynomial computational complexity, motivating interest in quantum algorithms that may provide asymptotic computational advantages under appropriate assumptions regarding sparsity, conditioning, and state preparation. In particular, the Harrow–Hassidim–Lloyd (HHL) algorithm [13] introduced the first quantum algorithm capable of preparing a quantum state proportional to the solution of a sparse linear system with polylogarithmic dependence on the problem dimension. Although practical performance depends upon factors such as matrix conditioning, sparsity, and quantum state preparation, HHL established the theoretical foundation for quantum linear-system solvers applicable to scientific computing.

Since its introduction, substantial advances have extended the capabilities of quantum linear-system algorithms. Childs *et al.* [14] developed improved formulations exhibiting

polynomial dependence on solution precision, while Berry *et al.* [15] introduced quantum algorithms for directly solving systems of linear differential equations. More recent investigations have explored the application of quantum linear-system algorithms to finite-difference, finite-element, and time-dependent PDE formulations, demonstrating the potential of quantum computing for large-scale scientific and engineering simulation [15–19].

Despite these advances, relatively little work has explored the integration of wavelet-based multiresolution analysis with quantum linear-system algorithms within a unified computational framework. In particular, the combination of Haar multiresolution analysis, Schur-complement reduction, and quantum linear-system inversion offers the opportunity to combine complementary reductions in classical problem size with improved conditioning prior to quantum inversion. By reducing the dimensionality and improving the conditioning of the discretized system prior to quantum inversion, the multiresolution hierarchy provides a natural preprocessing stage for quantum linear-system algorithms [9–12].

The present work introduces a hybrid wavelet–Schur–HHL framework for the solution of linear partial differential equations. Building upon the author's previous work in Haar-based multiresolution discretization and Schur-complement reduction [9], the proposed methodology embeds the condensed wavelet–Schur system directly within the Harrow–Hassidim–Lloyd quantum linear-system algorithm [13]. Unlike existing quantum PDE formulations, which typically apply HHL directly to finite-difference or finite-element discretizations, the proposed approach first performs multiresolution decomposition and Schur-complement reduction before executing the quantum inversion. Consequently, the quantum solver operates on a substantially smaller Schur-reduced system while preserving the multiscale information contained within the original discretization.

The scope of the present study is intentionally restricted to problem sizes that remain tractable on classical hardware, thereby enabling the proposed hybrid framework to be evaluated independently of current quantum hardware limitations. Within this setting, the present work makes three principal contributions. First, a Haar-based multiresolution formulation is developed in which Schur-complement reduction produces a compact condensed system that is well suited for quantum linear-system inversion. Second, the Harrow–Hassidim–Lloyd (HHL) algorithm is integrated directly within the Wavelet–Schur framework to create a unified hybrid quantum–classical solution methodology that preserves the hierarchical structure of the underlying multiresolution discretization. Third, the proposed framework is demonstrated on representative one- and two-dimensional elliptic and hyperbolic partial differential equations, with systematic comparisons against finite-difference reference solutions, classical wavelet–Schur reconstructions, and quantum resource requirements. Collectively, these results establish a unified Wavelet–Schur–HHL computational framework that demonstrates the feasibility of combining multiresolution wavelet discretization, Schur-complement reduction, and quantum linear-system algorithms within a single hybrid methodology.

2. Method

2.1 Governing Equations and Classical Multiresolution Framework

The present work considers linear partial differential equations represented by the general boundary-value problem

$$L(u) = f, u\,|_{\partial\Omega} = g, (x,t) \in \Omega \times [0,T], \tag{1}$$

where $L(\cdot)$ denotes a linear differential operator, $u(x,t)$ is the unknown solution field, $f(x,t)$ is a prescribed forcing function, and $g(x,t)$ specifies the corresponding boundary conditions [2]. This formulation encompasses a broad class of governing equations arising in computational mechanics, fluid dynamics, structural analysis, heat transfer, and wave propagation. Representative benchmark problems considered in this work belong to three canonical classes of partial differential equations:

Elliptic (Poisson equation)

$$-\nabla^2 u(x) = f(x), u\,|_{\partial\Omega} = g(x), \tag{2}$$

Parabolic (Diffusion equation)

$$\frac{\partial u(x,t)}{\partial t} - \nabla^2 u(x,t) = f(x,t), u(x,0) = u_0(x), \tag{3}$$

Hyperbolic (Wave equation)

$$\frac{\partial^2 u(x,t)}{\partial t^2} - c^2\nabla^2 u(x,t) = f(x,t), u(x,0) = u_0(x), \frac{\partial u}{\partial t} = v_0(x). \tag{4}$$

Although all three equation classes are introduced for completeness, the numerical benchmarks presented later focus primarily on elliptic and hyperbolic systems. Time-dependent problems are discretized using second-order finite-difference or Crank–Nicolson-type schemes, reducing each time level to the solution of a sparse linear algebraic system.

Application of standard finite-difference discretization converts Eqs. (2)–(4) into the sparse linear algebraic system

$$\mathbf{Ax} = \mathbf{b}, \tag{5}$$

where **A** denotes the discretized differential operator, $x$contains the unknown nodal solution values, and **b** represents the source vector together with the imposed boundary conditions. For a nodal finite-difference discretization,

$$\mathbf{x} = \begin{bmatrix} u_h(\mathbf{r}_1, t) \\ u_h(\mathbf{r}_2, t) \\ \vdots \\ u_h(\mathbf{r}_N, t) \end{bmatrix}, \tag{6}$$

where r_i denotes the i^{th} spatial grid point and u_h is the discrete approximation to the continuous solution.

Rather than solving Eq. (5) directly in the nodal basis, the present work transforms the discrete system into a hierarchical multiresolution representation using an orthogonal Haar wavelet basis. The corresponding continuous approximation is expressed as

$$u_h(\mathbf{r}, t) = \sum_k c_{0,k}(t)\phi_{0,k}(\mathbf{r}) + \sum_{j=0}^{r_{max}-1} \sum_k d_{j,k}(t)\psi_{j,k}(\mathbf{r}), \tag{7}$$

where $\phi_{0,k}$ and $\psi_{j,k}$ denote the Haar scaling and wavelet basis functions, respectively [3–9]. The scaling coefficients $c_{0,k}$ capture the large-scale behavior of the solution, whereas the wavelet coefficients $d_{j,k}$ successively resolve finer spatial features. This hierarchical decomposition provides a compact representation that naturally separates solution behavior across multiple spatial scales. Consequently, smooth solution behavior is represented primarily by the scaling coefficients, while localized gradients and fine-scale features are captured by the wavelet coefficients.

For numerical implementation, the continuous expansion of Eq. (7) is represented through the discrete orthogonal Haar transform

$$\hat{\mathbf{x}} = \mathbf{W}\mathbf{x} = \begin{bmatrix} \mathbf{x}_c \\ \mathbf{x}_f \end{bmatrix}, \tag{8}$$

where $\mathbf{W}$ is the orthogonal Haar transformation matrix, $\mathbf{x}_c$ contains the coarse-scale scaling coefficients, and $\mathbf{x}_f$ contains the fine-scale wavelet coefficients. Consequently, Eqs. (6)–(8) establish the connection between the physical nodal solution and its equivalent multiresolution representation.

Applying the orthogonal Haar transformation to Eq. (5) yields

$$\widehat{\mathbf{A}} = \mathbf{W}\mathbf{A}\mathbf{W}^T, \hat{\mathbf{b}} = \mathbf{W}\mathbf{b}, \tag{9}$$

where

$$\mathbf{W}\mathbf{W}^T = \mathbf{W}^T\mathbf{W} = \mathbf{I}, \tag{10}$$

yielding the transformed linear system

$$\widehat{\mathbf{A}}\hat{\mathbf{x}} = \hat{\mathbf{b}}. \tag{11}$$

The transformed operator [7] naturally partitions into coarse- and fine-scale subspaces

$$\begin{bmatrix} \widehat{\mathbf{A}}_{cc} & \widehat{\mathbf{A}}_{cf} \\ \widehat{\mathbf{A}}_{fc} & \widehat{\mathbf{A}}_{ff} \end{bmatrix} \begin{bmatrix} \mathbf{x}_c \\ \mathbf{x}_f \end{bmatrix} = \begin{bmatrix} \mathbf{b}_c \\ \mathbf{b}_f \end{bmatrix}, \tag{12}$$

where $\widehat{\mathbf{A}}_{cc}$ and $\widehat{\mathbf{A}}_{ff}$ describe interactions within the scaling and wavelet subspaces, respectively, while the off-diagonal blocks account for coupling between the two resolution levels.

To reduce the dimensionality of the system passed to the quantum solver, the fine-scale wavelet-detail coefficients are eliminated through Schur-complement reduction [10–12]. The resulting condensed system retains the coarse-scale scaling coefficients while incorporating the influence of the eliminated fine-scale variables. Specifically, the Schur-complement operator is defined as

$$\mathbf{S} = \widehat{\mathbf{A}}_{cc} - \widehat{\mathbf{A}}_{cf}\widehat{\mathbf{A}}_{ff}^{-1}\widehat{\mathbf{A}}_{fc}, \tag{13}$$

where $\mathbf{S} \in \mathbb{R}^{n_c \times n_c}$, and $\widehat{\mathbf{A}}_{ff}$ is assumed nonsingular. The corresponding reduced right-hand-side vector is

$$b_S = \hat{b}_c - \widehat{\mathbf{A}}_{cf}\widehat{\mathbf{A}}_{ff}^{-1}\hat{b}_f \, . \tag{14}$$

The coarse-scale coefficients are obtained from the reduced system

$$\mathrm{S}\mathbf{x}_c = \mathbf{b}_S. \tag{15}$$

Following the reduced-system solution, the eliminated fine-scale coefficients are recovered classically according to

$$\mathbf{x}_f = \widehat{\mathbf{A}}_{ff}^{-1}\left(\hat{b}_f - \widehat{\mathbf{A}}_{fc}\mathbf{x}_c\right). \tag{16}$$

The complete physical-space solution is then reconstructed through the inverse Haar transformation,

$$x = \mathbf{W}^T \begin{bmatrix} x_c \\ x_f \end{bmatrix}. \tag{17}$$

The wavelet–Schur formulation therefore transforms the original finite-difference discretization into a lower-dimensional condensed system while preserving the influence

of the eliminated fine-scale variables. By reducing both the size and, in many cases, the conditioning of the linear system prior to quantum inversion, the multiresolution framework provides an efficient classical preprocessing stage for the quantum algorithm. Consequently, the HHL solver operates only on the condensed Schur system rather than the full discretized operator. This wavelet–Schur reduction constitutes the key classical component of the hybrid Wavelet–Schur–HHL methodology developed in this work.

2.2. Hybrid Wavelet–Schur–HHL Framework

Following the Haar multiresolution transformation and Schur-complement reduction described in Section 2.1, the original discretized partial differential equation is reduced to a condensed linear system involving only the coarse-scale wavelet coefficients. This reduced system forms the input to the quantum linear-system solver. Consequently, the proposed methodology combines classical multiresolution reduction with quantum inversion, allowing the computationally intensive linear solve to be performed within the quantum stage while all preprocessing and reconstruction operations remain classical. The condensed Schur system is

$$\mathbf{S}\mathbf{x}_c = \mathbf{b}_S, \tag{18}$$

where $\mathbf{S} \in \mathbb{R}^{n_c \times n_c}$ denotes the wavelet-domain Schur operator, $\mathbf{x}_c$ contains the unknown coarse-scale scaling coefficients, and $\mathrm{b}_S$is the corresponding condensed right-hand-side vector.

The Harrow–Hassidim–Lloyd (HHL) algorithm [13] requires the system operator supplied to quantum phase estimation to be Hermitian. When the Schur operator is Hermitian, Eq. (18) may be used directly. Otherwise, the condensed system is converted into the equivalent Hermitian block form

$$\mathbf{H}_S = \begin{bmatrix} 0 & \mathbf{S} \\ \mathbf{S}^\dagger & 0 \end{bmatrix}, \tag{19}$$

with the augmented vectors

$$\tilde{\mathbf{x}} = \begin{bmatrix} 0 \\ \mathbf{x}_c \end{bmatrix}, \tilde{\mathbf{b}} = \begin{bmatrix} \mathbf{b}_S \\ 0 \end{bmatrix}, \tag{20}$$

such that

$$\mathbf{H}_S\tilde{\mathbf{x}} = \tilde{\mathbf{b}}. \tag{21}$$

The Hermitian block embedding provides a general formulation for Schur operators that are not inherently Hermitian. For benchmark operators that are symmetric, the numerical implementation may instead employ the Schur matrix directly, with numerical symmetrization used only to suppress roundoff-level asymmetry. The resulting operator is examined spectrally to determine whether positive-definite, negative-definite, or signed eigenvalue inversion is appropriate. For nonsymmetric operators, including the one-dimensional advection benchmark,

the Hermitian block embedding is used to preserve the original Schur system without introducing an approximation through symmetrization.

For the one-dimensional advection benchmark, the Schur-complement operator is nonsymmetric because of the directional transport terms. Consequently, direct symmetrization would alter the discrete operator and is not employed. Instead, the Schur system is represented using the Hermitian block embedding of Eq. (19), with the augmented right-hand side defined by Eq. (20). The eigenvalues of the embedded operator are treated with their signs retained during reciprocal-eigenvalue encoding. This formulation preserves the original nonsymmetric Schur system while satisfying the Hermiticity requirement of quantum phase estimation. The desired coarse-scale coefficient vector is recovered from the corresponding block of the post-selected HHL solution state.

The Hermitian embedding preserves the solution of the original Schur system while satisfying the Hermiticity requirement of the HHL algorithm. For simplicity, the Hermitian operator supplied to the quantum solver is denoted by **H**, irrespective of whether it corresponds directly to the Schur operator or to the block embedding of Eq. (19).
The normalized right-hand-side vector is encoded as the quantum state [13]

$$|\mathbf{b}\rangle = \frac{1}{\|\mathbf{b}_H\|_2} \sum_j (b_H)_j |\mathrm{j}\rangle, \tag{22}$$

where

$$\mathbf{b}_H = \begin{cases} \mathbf{b}_S, & \text{if } \mathbf{S} \text{ is Hermitian,} \\ \tilde{\mathbf{b}}, & \text{otherwise.} \end{cases} \tag{23}$$

Quantum phase estimation is subsequently performed through controlled time evolution under the unitary operator

$$\mathrm{U} = e^{i\mathbf{H}\tau}, \tag{24}$$

which decomposes the input state into the eigenbasis of the system operator,

$$\sum_i c_i \, |\mathbf{u}_i\rangle \, | \, \tilde{\lambda}_i\rangle, \tag{25}$$

where

$$\mathbf{H}|u_i\rangle = \lambda_i |\mathbf{u}_i\rangle, \qquad |\mathbf{b}\rangle = \sum_i c_i \, |\mathbf{u}_i\rangle. \tag{26}$$

The eigenvalues encoded in the phase-estimation register are then used to perform the controlled ancilla rotation

$$|\tilde{\lambda}_i\rangle|0\rangle \rightarrow |\tilde{\lambda}_i\rangle\left[\sqrt{1-\left(\frac{C}{\lambda_i}\right)^2}\,|0\rangle + \frac{C}{\lambda_i}|1\rangle\right], \tag{27}$$

where C is selected such that $0 < C/|\,\lambda_i\,| \leq 1$ over the retained eigenvalue spectrum [13]. This operation encodes the reciprocal eigenvalues without explicitly forming the inverse of the system matrix.

Following inverse quantum phase estimation and successful postselection of the ancilla qubit in the state $|1\rangle$, the quantum register contains the normalized solution

$$|\mathbf{x}_H\rangle \propto \sum_i \frac{c_i}{\lambda_i}|\mathbf{u}_i\rangle. \tag{28}$$

When the Hermitian block embedding is employed, the desired coarse-scale solution vector x_c is extracted from the appropriate block of the recovered quantum state. The eliminated fine-scale coefficients are then reconstructed classically using

$$\widehat{\mathbf{A}}_{ff}\mathbf{x}_f = \hat{b}_f - \widehat{\mathbf{A}}_{fc}\mathbf{x}_c, \tag{29}$$

and the complete nodal solution is recovered through the inverse Haar transformation,

$$\mathbf{x} = \mathbf{W}^T\begin{bmatrix}\mathbf{x}_c \\ \mathbf{x}_f\end{bmatrix}. \tag{30}$$

The resulting procedure constitutes a complete hybrid Wavelet–Schur–HHL computational framework in which Haar multiresolution analysis and Schur-complement reduction provide efficient classical preprocessing, the HHL algorithm performs the quantum linear-system inversion, and the final physical-space solution is recovered through inverse wavelet reconstruction. This hybrid workflow forms the computational basis for the numerical benchmarks presented in the following section.

2.3 Quantum Circuit Implementation

The quantum inversion stage of the proposed Wavelet–Schur–HHL framework is implemented using the standard Harrow–Hassidim–Lloyd (HHL) circuit architecture [13] illustrated schematically in Figure 1. The circuit operates on the Schur-complement system derived in Section 2.2 and consists of four principal stages: state preparation, quantum phase estimation, controlled eigenvalue inversion, and inverse phase estimation [21].

The vector register is initialized to the normalized right-hand-side state associated with the Hermitian operator supplied to the quantum solver, using either the original Schur right-hand side or its augmented counterpart for the Hermitian block embedding. Controlled applications of the unitary operator

$$U = e^{i\mathbf{H}\tau}, \tag{31}$$

are used during quantum phase estimation, where H denotes the Hermitian operator supplied to the quantum solver, corresponding either to the Schur operator itself or to the Hermitian block embedding defined in Eq. (19). This stage decomposes the input state into the eigenbasis of the operator while encoding approximate eigenvalues in the auxiliary register. This stage transforms the input state into the eigenbasis of the operator while simultaneously recording approximate eigenvalues in the auxiliary register.

Following quantum phase estimation, an inverse quantum Fourier transform converts the encoded eigenphases into a binary representation suitable for controlling a sequence of ancilla rotations. The resulting multi-controlled R_y operation approximately applies the reciprocal eigenvalue transformation required for matrix inversion, thereby implementing the central operation of the HHL algorithm. Following the ancilla rotation, the inverse phase-estimation circuit is applied to return the phase register to its initial state, leaving the vector and ancilla registers in a joint quantum state.

Finally, measurement and postselection of the ancilla qubit in the state $|1\rangle$ yield a quantum state proportional to the coarse-scale solution of the Schur system. The recovered wavelet coefficients are subsequently rescaled, combined with the classically reconstructed fine-scale coefficients, and transformed back to the physical domain through the inverse Haar transform described in Section 2.2. The same circuit architecture is employed for all benchmark problems; only the Schur operator and corresponding right-hand-side vector differ between individual PDEs.

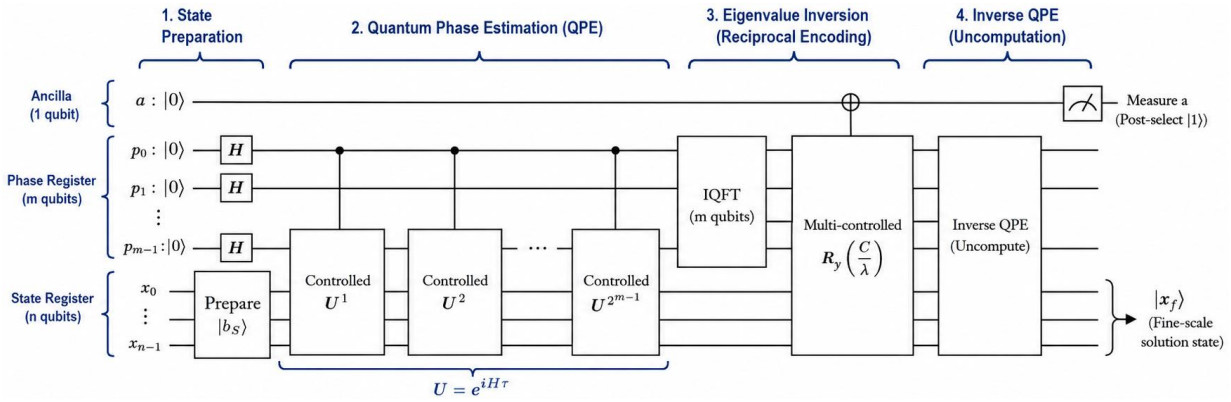


Fig. 1 Quantum circuit implementing the HHL inversion stage of the proposed Wavelet–Schur–HHL framework**.** The vector register is initialized to the normalized right-hand-side state associated with the Hermitian operator supplied to the quantum solver, using either the original Schur right-hand side or its augmented counterpart for the Hermitian block embedding**.** Following the inverse quantum Fourier transform, a multi-controlled R_y rotation on the ancilla encodes approximate reciprocal eigenvalues. The inverse phase-estimation circuit is then applied to return the phase register to its initial state. Following successful ancilla postselection, the vector register encodes

a state proportional to the coarse-scale Schur solution, from which the complete physical-space solution is recovered through the classical wavelet–Schur reconstruction procedure.

Following quantum phase estimation, controlled eigenvalue inversion, and uncomputation, the HHL solution is recovered from the noiseless simulated statevector by postselecting the ancilla qubit in state $|1\rangle$ and the phase register in state $|0 \ldots 0\rangle$. The resulting amplitude vector is normalized and transformed back to the physical coefficient ordering using the inverse register permutation. Because the recovered quantum state specifies the solution direction rather than its absolute magnitude, a least-squares scaling factor is determined by minimizing the residual of the Schur-reduced system:

$$\alpha_S = \frac{(\mathbf{S}\hat{\mathbf{x}}_S)^T \mathbf{b}_S}{\|\mathbf{S}\hat{\mathbf{x}}_S\|_2^2} . \tag{32}$$

The initial classical approximation is then

$$\mathbf{x}_S^{(0)} = \alpha_S \hat{\mathbf{x}}_S . \tag{33}$$

For the nonsymmetric advection benchmark, a separate amplitude-calibration procedure was used. Because the HHL statevector determines the solution direction but not its absolute magnitude, the recovered coefficient vector was scaled by a least-squares factor minimizing its Euclidean difference from the independently computed classical Schur solution. This reference-based calibration was used exclusively for the reported advection validation and differs from the residual-minimizing scaling defined in Eq. (32). The resulting errors therefore quantify the agreement of the calibrated HHL solution direction with the classical Schur solution, rather than the accuracy of an independently normalized quantum output.

For the one-dimensional Poisson and forced-oscillator benchmark problems, the recovered approximation is further refined using a limited number of conjugate-gradient iterations applied to the Schur-reduced system, with the initial residual defined as

$$\mathbf{r}^{(0)} = \mathbf{b}_S - \mathbf{S}\mathbf{x}_S^{(0)}. \tag{34}$$

The iterations terminate when

$$\left\|\mathbf{r}^{(k)}\right\|_2^2 < 10^{-14} , \tag{35}$$

or when the prescribed maximum iteration count is reached. The Poisson and forced-oscillator benchmarks use maximum iteration counts of six and two, respectively. Following refinement, the eliminated wavelet coefficients are recovered through classical back-substitution, and the full solution is reconstructed using the inverse Haar transformation. A final scalar correction

along an HHL-derived reconstruction direction minimizes the residual of the original discretized system.

2.4. Computational Complexity and Quantum Resource Requirements

One of the principal advantages of incorporating Schur-complement reduction within the proposed Wavelet–Schur–HHL framework is that the quantum solver operates only on the condensed coarse-scale system rather than the full discretized operator. This reduction decreases the dimension of the linear system while retaining the influence of the eliminated wavelet-detail coefficients through the Schur-complement operator. For the benchmark problems considered in this study, the Schur-complement operator consistently exhibited condition numbers approximately two to three times smaller than those of the corresponding full system matrices. Because the performance of HHL-type quantum linear-system algorithms depends strongly on both the dimension and conditioning of the system operator, the reduced size and improved conditioning of the Schur system provide a more favorable target for quantum inversion than the unreduced finite-difference discretization. These observations are consistent with the theoretical complexity of HHL, which exhibits only polylogarithmic dependence on problem dimension while remaining sensitive to the condition number of the system matrix [13–15].

All quantum calculations were performed using noiseless statevector simulation. The HHL circuit consists of a vector register, a phase-estimation register, and one ancilla qubit. For a Schur-reduced system of dimension N_S, the vector register requires $n_v = [log_2(N_S)]$ qubits. When Hermitian block embedding is required for a nonsymmetric Schur operator, the system dimension increases from N_S to $2N_S$. Accordingly, the vector register requires $[\log_2(2N_S)]$ qubits, corresponding to one additional qubit when N_S is a power of two. The number of phase-estimation qubits is selected adaptively according to the normalized eigenvalue spectrum, with a minimum of eight and a maximum of twelve qubits in the one-dimensional Poisson and forced-oscillator implementations. The total circuit size is therefore $n_{total} = n_v + n_{phase} + 1$. For the discretizations considered in these two benchmarks, the resulting circuit sizes range from 10 to 17 qubits. These counts describe the logical registers used in the statevector simulations and do not represent gate-level resource estimates for fault-tolerant quantum hardware.

For the present proof-of-concept implementation, controlled applications of the unitary operator

$$U = e^{iH\tau}, \tag{36}$$

were realized through exact matrix exponentiation within the simulator. Consequently, the reported solution accuracy and algorithmic behavior reflect the proposed Wavelet–Schur–HHL methodology rather than the performance limitations of current quantum hardware.

Practical quantum implementations will additionally incur the computational costs associated with Hamiltonian simulation, block encoding, and fault-tolerant quantum error correction [16–20]. Consequently, the present simulations should be viewed as an algorithmic benchmark that isolates the effectiveness of wavelet multiresolution reduction and Schur-

complement condensation within a hybrid quantum–classical PDE solver, thereby providing a reproducible baseline for future implementations on fault-tolerant quantum hardware.

All quantum computations reported in this study were performed using noiseless Qiskit simulation. The HHL solution amplitudes were obtained directly from the simulated statevector by selecting the ancilla-success subspace and the zero-phase-register component following quantum phase estimation and uncomputation. The resulting amplitudes were subsequently rescaled and incorporated into the classical Schur-complement reconstruction and residual-based refinement procedures. Separately, representative measurement-count distributions were generated using 4,096 simulated circuit shots to illustrate the probability distribution over computational basis states. These measurement histograms serve as diagnostic visualizations and were not used to estimate the solution amplitudes or construct the reported numerical solutions. Consequently, the results characterize the numerical behavior of the hybrid algorithm under idealized statevector simulation rather than the performance of a finite-shot quantum hardware implementation.

The present study is intended to establish the numerical feasibility of integrating Haar-wavelet multiresolution reduction, Schur-complement elimination, and HHL-based quantum linear-system inversion, rather than to demonstrate an end-to-end quantum computational speedup. Although the Schur reduction decreases the dimension of the system presented to the quantum solver and may improve its spectral conditioning, these properties do not, by themselves, establish a reduction in total computational complexity. The construction of the Schur complement requires classical preprocessing and may introduce matrix fill-in, while practical quantum implementations incur additional costs associated with state preparation, Hamiltonian simulation, postselection, and solution readout. Moreover, the present implementation uses noiseless statevector simulation and exact matrix exponentiation, which permit controlled examination of the hybrid numerical formulation but do not represent the resource requirements of a fault-tolerant quantum implementation. Accordingly, the reported reductions in system dimension and condition number should be interpreted as favorable numerical characteristics of the proposed framework, rather than as direct evidence of quantum computational advantage.

3. Results

3.1. One-Dimensional Boundary-Value Benchmark Problems

To evaluate the proposed Wavelet–Schur–HHL framework, three representative one-dimensional boundary-value problems were selected to investigate the performance of the hybrid algorithm over a range of operator and solution characteristics. The benchmark suite consists of a classical Poisson problem with a smooth solution, a forced-oscillator problem exhibiting oscillatory behavior, and an exponentially forced boundary-value problem. Together, these examples provide complementary test cases for assessing the accuracy of the wavelet–Schur

decomposition and subsequent quantum inversion of the reduced Schur system. The governing equations are

$$\frac{d^2y(x)}{dx^2} + 1 = 0, \quad x \in [0,1], \quad y(0) = y(1) = 0, \tag{37}$$

$$\frac{d^2x(t)}{dt^2} + x = 5\cos(4t), \quad t \in [0,6], \quad x(0) = 1, \quad x(6) = 0.5, \tag{38}$$

$$\frac{d^2\phi(r)}{dr^2} = -\frac{re^{-r}}{2}, \quad r \in [0,\infty), \quad \phi(0) = 0, \quad \phi(\infty) = 1. \tag{39}$$

For the exponentially forced boundary-value problem in Eq. (39), the semi-infinite domain was truncated to the finite interval $0 \le r \le 20$, with the far-field condition approximated by imposing $\varphi(20) = 1$. The analytical reference solution was evaluated for this truncated boundary-value problem, thereby providing a consistent basis for comparison with the finite-difference and hybrid wavelet–Schur–HHL solutions. The maximum difference between the truncated-domain analytical solution and its semi-infinite counterpart is approximately 2.27×10^{-8} over the computational interval, indicating that the selected domain length introduces negligible truncation error for the present benchmark.

Each problem was first solved using a second-order finite-difference discretization to generate a high-resolution reference solution. Classical wavelet–Schur reconstructions and the corresponding hybrid HHL–CG solutions were subsequently computed over dyadic refinement levels with interior problem sizes ranging from 8 to 32 degrees of freedom (DOF). For each benchmark, the Schur complement was assembled from the wavelet-transformed operator and supplied to the HHL solver described in Section 2.2. The recovered quantum approximation was then incorporated into the hybrid reconstruction through the residual-based conjugate-gradient refinement procedure described previously.

To illustrate the operation of the simulated HHL quantum inversion stage, Figure 2 presents representative measurement statistics and recovered statevector amplitudes for the Poisson benchmark at an intermediate refinement level. Figure 2(a) shows the distribution of computational-basis measurement outcomes obtained from 4,096 simulated circuit shots, while Figure 2(b) presents the real amplitudes extracted from the noiseless statevector following selection of the ancilla-success and zero-phase-register subspace. The measurement distribution provides a diagnostic representation of the circuit's output probabilities, whereas the statevector amplitudes provide the solution information used in the subsequent classical reconstruction. These results illustrate the expected behavior of the simulated HHL circuit but should not be interpreted as demonstrating finite-shot solution recovery or quantum hardware performance.

Figure 3 compares the exact analytical solutions, the fine-grid finite-difference reference solutions, the classical wavelet–Schur reconstructions, and the corresponding hybrid HHL–CG solutions for the three benchmark problems. Quantitative accuracy metrics for each benchmark are summarized in Table 1.

As shown in Table 1, the wavelet–Schur preprocessing consistently reduced the condition number of the condensed Schur system by approximately a factor of two for all benchmark problems and discretization levels. This reduction was largely independent of the governing differential equation and depended primarily on the multiresolution discretization, indicating that the conditioning improvement is an inherent property of the wavelet–Schur decomposition rather than the particular elliptic operator. The table also summarizes the relative L_2errors of both the classical and hybrid reconstructions, providing a concise comparison of the numerical performance across the three benchmark problems.

The Poisson equation serves primarily as a verification benchmark because of its smooth analytical solution and well-characterized discretized operator. As illustrated in Figure 3(a), the classical wavelet–Schur reconstruction closely reproduces the finite-difference reference solution across the refinement levels considered. The hybrid HHL–CG reconstruction also exhibits good agreement at the smaller discretizations, with relative L2 errors of 1.71×10^{-15} and 4.90×10^{-13} for 8 and 16 degrees of freedom, respectively. At 32 degrees of freedom, however, the hybrid relative L2 error increases to 4.74×10^{-4}, compared with 3.71×10^{-15} for the classical reconstruction. This discrepancy indicates a loss of accuracy in the hybrid inversion and refinement procedure at the largest discretization examined, despite the continued reduction in the Schur-system condition number. Thus, while the Poisson results demonstrate the feasibility of the hybrid reconstruction, they also highlight the sensitivity of the HHL-based approximation to numerical resolution and the importance of controlling the accuracy of the quantum inversion stage.

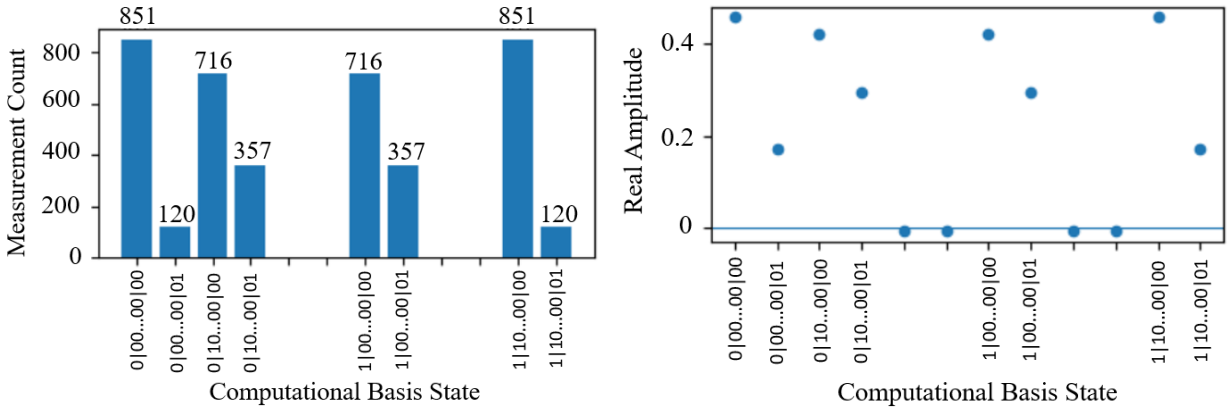
The forced oscillator represents a more demanding benchmark because the oscillatory forcing introduces higher-frequency solution content that is more difficult to represent on coarse multiresolution grids. As shown in Figure 3(b), the lowest-resolution approximation exhibits noticeable deviations from the reference solution, while both the classical and hybrid reconstructions improve systematically as additional wavelet levels are introduced. At the intermediate and finest discretizations, both approaches closely follow the finite-difference reference, with the hybrid reconstruction producing a slightly smaller relative L_2error at the highest resolution. These results demonstrate that the proposed framework maintains competitive accuracy even for operators containing significant oscillatory behavior.

The exponential-source problem represents the most challenging benchmark because the exponentially decaying source term produces stronger global coupling throughout the Schur system. Figure 3(c) shows that both reconstructions approach the exact solution as the discretization is refined; however, the raw HHL approximation alone is insufficient to recover the classical solution at the finer discretizations. Residual-based conjugate-gradient refinement rapidly reduces the Schur-system residual and restores the classical wavelet–Schur solution for every problem size considered, as reflected by the identical relative L_2errors reported in Table 1. These results demonstrate that the hybrid HHL–CG formulation effectively combines quantum inversion with classical iterative refinement, allowing the quantum approximation to serve as an initial estimate while preserving the accuracy of the classical multiresolution solution.

Collectively, these benchmark problems demonstrate the correctness and robustness of the proposed Wavelet–Schur–HHL framework across representative one-dimensional elliptic operators. The consistent agreement between the classical and hybrid reconstructions establishes the proposed methodology as a viable hybrid quantum–classical approach for multiresolution solution of linear partial differential equations.

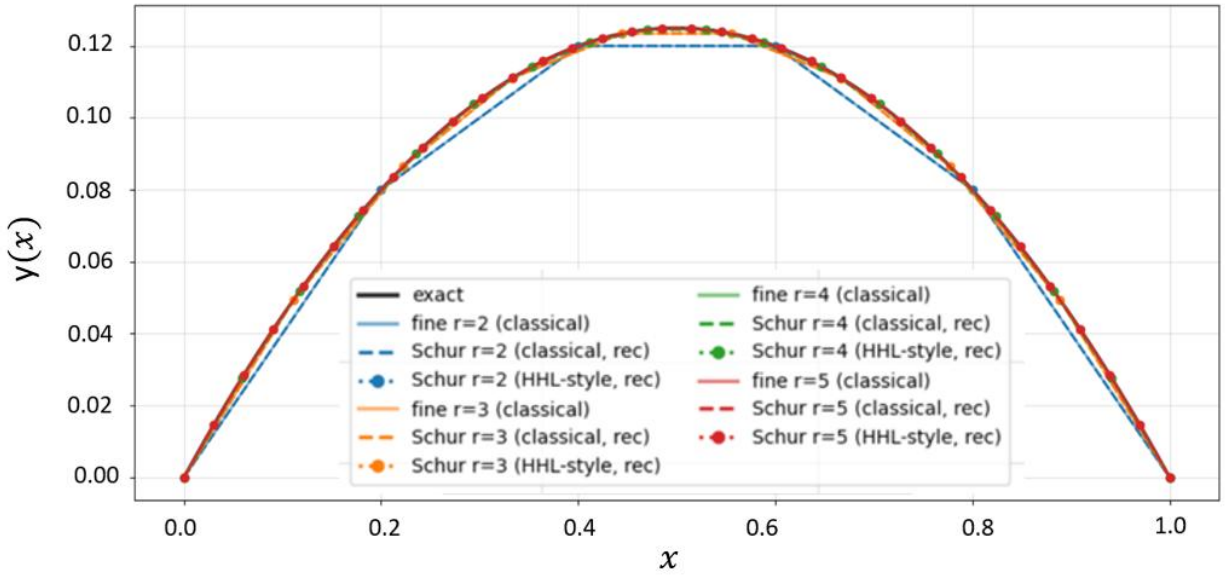
Table 1. Comparison of relative L_2 errors and conditioning reduction factors for classical wavelet–Schur and hybrid HHL–CG solutions across three one-dimensional boundary-value benchmark problems.

Benchmark	**Degrees of Freedom (DOF)**	**Classical Schur Rel. L_2 Error**	**Hybrid HHL-CG Rel. L_2 Error**	**Conditioning Reduction κ(A)/ κ (S)**	**Observation**
Poisson	8	3.29×10^{-16}	1.71×10^{-15}	2.282	Verification case
	16	7.06×10^{-16}	4.90×10^{-13}	2.099	Classical agreement maintained
	32	3.71×10^{-15}	4.74×10^{-4}	2.030	Hybrid error increases with DOF
Oscillator	8	1.089399	1.103899	2.932	Hybrid closely matches classical
	16	0.173713	0.189429	2.227	Hybrid closely matches classical
	32	0.040700	0.038920	2.061	Hybrid slightly lower L_2 error
Exponential	8	0.031990	0.031990	2.282	Classical recovered after CG
	16	0.005089	0.005089	2.099	Classical recovered after CG
	32	0.001637	0.001637	2.030	Classical recovered after CG

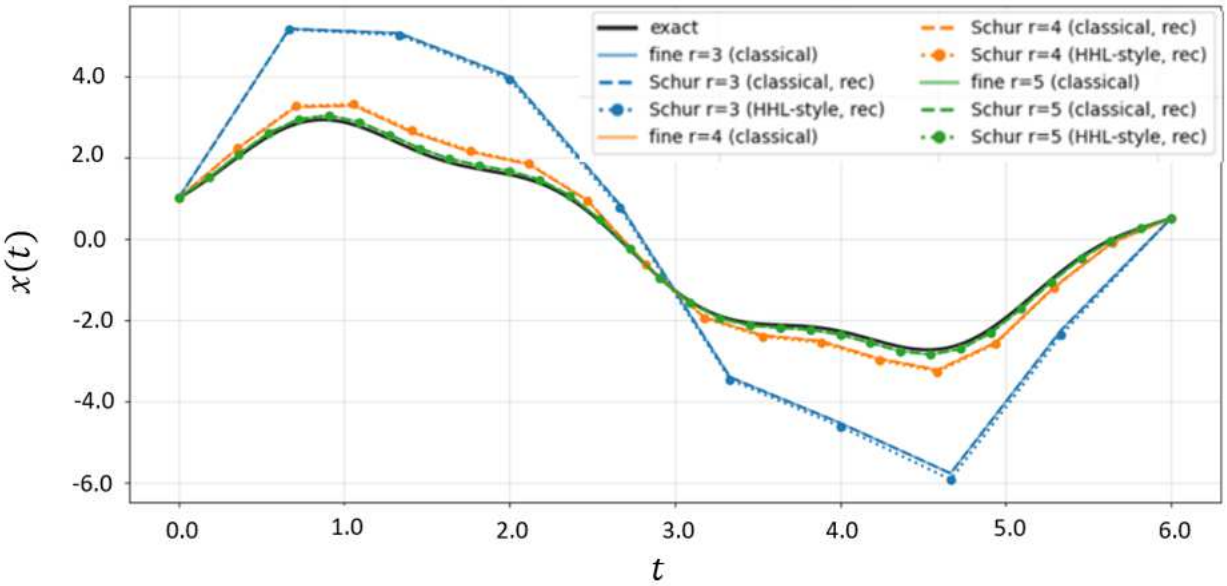


(a) Measurement Statistics (b) Recovered Solution Amplitudes

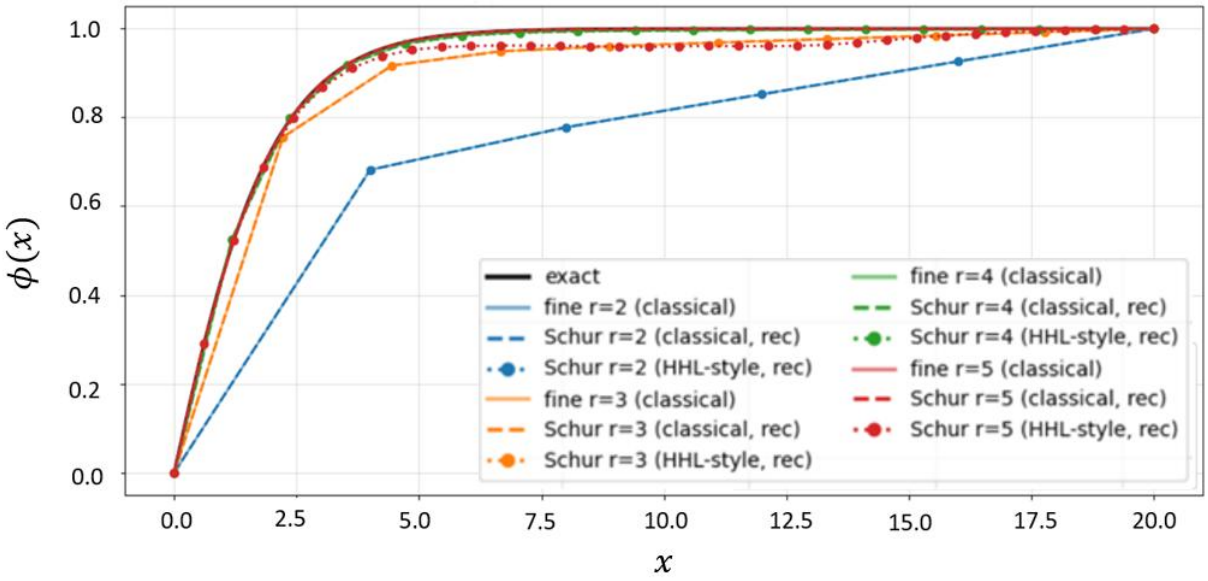
Fig. 2 Representative HHL simulation diagnostics for the one-dimensional Poisson benchmark. (a) Computational-basis measurement counts obtained from 4,096 simulated shots. (b) Real amplitudes extracted from the noiseless statevector following selection of the ancilla-success and zero-phase-register subspace. The histograms provide circuit diagnostics, while the statevector amplitudes are used in the subsequent hybrid reconstruction.



(a) $\frac{d^2y(x)}{dx^2} + 1 = 0$



(b) $\frac{d^2x(t)}{dt^2} + x = 5\cos(4t)$



$$(c)\ \frac{d^2\phi(r)}{dr^2} = -rexp(-r)/2$$

Fig. 3 Solutions of three one-dimensional boundary-value benchmark problems comparing the exact reference, fine-grid finite-difference results, classical wavelet–Schur reconstructions, and the corresponding hybrid HHL–CG variants. Panels (a)–(c) show, respectively, a simple Poisson equation, a driven harmonic oscillator, and an exponentially decaying radial problem. The hybrid HHL–CG reconstructions remain in close agreement with the corresponding classical wavelet–Schur solutions while both approaches converge toward the finite-difference reference solution with increasing multiresolution level.

3.2. Two-Dimensional Elliptic Benchmark Problems

The proposed Wavelet–Schur–HHL framework was next extended to two-dimensional elliptic boundary-value problems to evaluate its performance for multidimensional systems. Two representative benchmark problems were considered: the Laplace equation and a Helmholtz-type elliptic equation defined on rectangular computational domains. The Laplace problem provides a classical harmonic benchmark with smooth interior behavior, whereas the Helmholtz-type problem introduces an additional reaction term that produces greater interior variation and a more demanding spectral structure. Together, these examples assess the ability of the proposed methodology to preserve the accuracy of the classical wavelet–Schur formulation while extending the hybrid quantum solution strategy to multidimensional PDEs. The governing equations are

$$\frac{\partial^2 U}{\partial x^2} + \frac{\partial^2 U}{\partial y^2} = 0, \quad (x, y) \in [0,1] \times [0,1], \tag{40}$$

subject to

$$U(0, y) = U(1, y) = 2, \qquad 0 < y < 1,$$
$$U(x, 0) = U(x, 1) = 4, \qquad 0 \le x \le 1,$$

and

$$\frac{\partial^2 U}{\partial x^2} + \frac{\partial^2 U}{\partial y^2} + U = 0, \quad (x, y) \in [-3,3] \times [-3,3], \tag{41}$$

with boundary condition

$$U(x, y) = \sin\left(\frac{\pi x}{6}\right), \quad (x, y) \in \partial\Omega.$$

The problem is defined on the unit square with prescribed Dirichlet boundary conditions of U = 2 along the open left and right edges and U = 4 along the upper and lower edges. Because these prescribed values differ at the corners, the boundary data are discontinuous at the four corner points. In the numerical implementation, the horizontal-edge boundary conditions take precedence, assigning U = 4 at all four corners. The finite-difference equations are assembled at the interior grid points, with boundary contributions incorporated into the right-hand-side vector. The same corner convention is applied to the finite-difference reference solution and both the classical and hybrid wavelet–Schur reconstructions.

High-resolution reference solutions were obtained using a second-order finite-difference discretization on uniform 64×64meshes solved by Gaussian elimination. Classical wavelet–Schur reconstructions and the corresponding hybrid HHL solutions were subsequently computed over dyadic multiresolution levels using Haar scaling and wavelet functions. At each refinement level, the two-dimensional Schur complement was assembled from the wavelet-transformed operator and embedded within the Hermitian system described in Section 2.2. The same HHL/QPE circuit architecture employed for the one-dimensional benchmarks was then used to solve the reduced Schur system, with the resulting quantum approximation incorporated into the multiresolution reconstruction. All solution fields were normalized by their maximum magnitude to facilitate direct comparison with the finite-difference reference solution.

To verify the operation of the quantum inversion stage for the two-dimensional problems, Figure 4 presents representative HHL diagnostics for the Laplace benchmark at refinement level $r = 3$. Figure 4(a) shows the measurement statistics for the most probable computational basis states obtained following quantum phase estimation and reciprocal-eigenvalue encoding. The measurement probability is concentrated within the dominant computational basis states, indicating that the primary spectral components of the Schur-reduced operator are captured efficiently by the quantum circuit. Figure 4(b) presents the corresponding recovered solution amplitudes obtained after post-selection of the ancilla qubit. The smooth variation of the dominant amplitudes is consistent with the harmonic nature of the Laplace solution and demonstrates that the HHL circuit produces the quantum state required for the subsequent hybrid reconstruction. Together, these diagnostics verify the expected behavior of the quantum inversion stage for the two-dimensional Schur system.

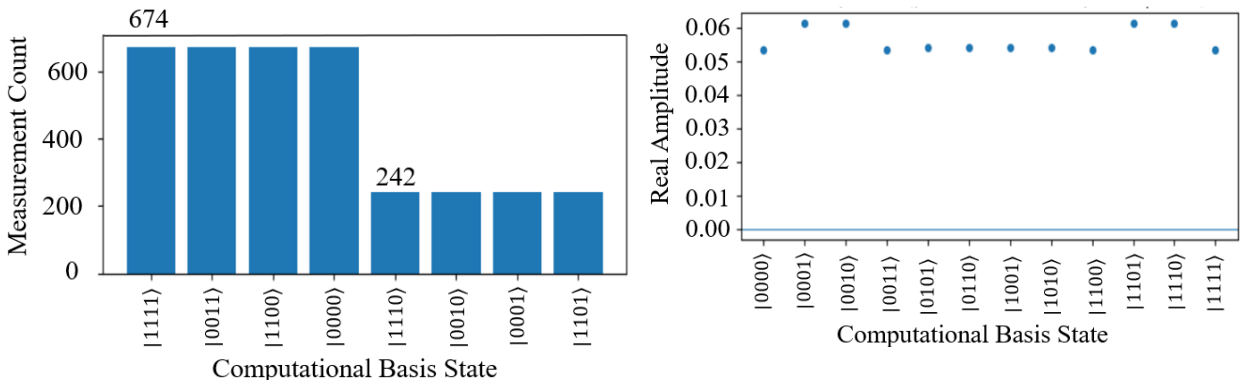
The numerical reconstructions obtained from the hybrid algorithm are presented in Figures 5 and 6. Figure 5 compares the finite-difference reference solution of the Laplace problem with the corresponding classical wavelet–Schur and hybrid HHL reconstructions

obtained at three representative multiresolution levels. At the coarsest scale, the reconstructed solution captures the dominant large-scale structure of the harmonic field while exhibiting the expected loss of spatial detail associated with aggressive wavelet compression. As additional wavelet levels are introduced, both the classical and hybrid reconstructions progressively recover the smooth curvature of the reference solution. Throughout the refinement process, the semi-transparent HHL surface remains in close agreement with the classical wavelet–Schur wireframe, indicating that the quantum inversion accurately reproduces the reduced Schur solution while preserving the convergence characteristics of the underlying multiresolution discretization.

Figure 6 demonstrates that the proposed methodology extends naturally to the Helmholtz-type elliptic problem. Relative to the Laplace benchmark, the reaction term produces stronger interior gradients and a more complex solution structure, resulting in a more demanding reconstruction problem. Nevertheless, both the classical and hybrid solutions converge systematically toward the finite-difference reference as the multiresolution level increases. At the coarser scales, the hybrid reconstruction accurately captures the dominant phase and amplitude characteristics of the solution, while successive refinement progressively recovers the remaining spatial detail. As observed for the Laplace problem, the close agreement between the HHL surface and the classical wavelet–Schur reconstruction indicates that the quantum inversion preserves the accuracy of the reduced Schur solution over a broader class of elliptic operators.

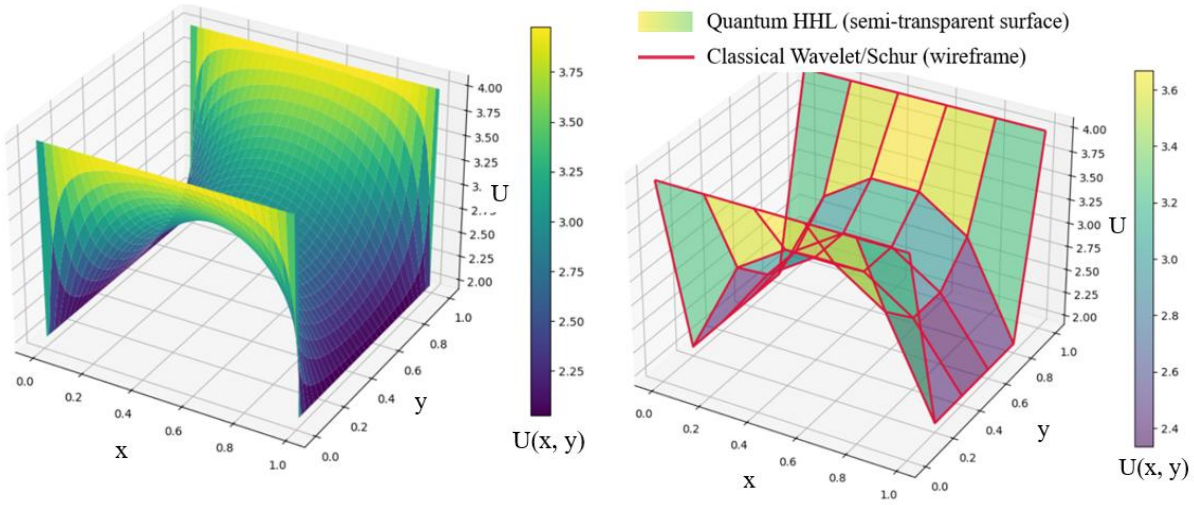
Quantitative error analysis further confirms the close agreement between the classical and hybrid reconstructions for the two-dimensional Helmholtz benchmark. At a discretization of 8×8 interior grid points, the relative L2 difference between the hybrid HHL reconstruction and the classical wavelet–Schur solution was 6.70×10^{-6}. The corresponding difference between the hybrid reconstruction and the direct finite-difference solution was also 6.70×10^{-6}, while the classical wavelet–Schur reconstruction agreed with the finite-difference solution to within 8.15×10^{-16}. These results demonstrate that the hybrid inversion and subsequent classical refinement reproduce the discrete Helmholtz solution with high accuracy at the resolution examined.

Collectively, the two-dimensional benchmark problems demonstrate that the proposed Wavelet–Schur–HHL framework extends naturally beyond one-dimensional test cases while maintaining the convergence characteristics of the underlying wavelet–Schur formulation. Figure 4 verifies the correct operation of the HHL inversion stage for the two-dimensional Schur system, whereas Figures 5 and 6 demonstrate that the resulting hybrid reconstructions converge systematically toward the finite-difference reference solutions for both harmonic and Helmholtz-type elliptic operators. The close agreement between the hybrid surfaces and the classical wavelet–Schur reconstructions across all refinement levels provides additional evidence that the proposed methodology accurately reproduces the reduced Schur solution while preserving the efficiency of the multiresolution representation. These multidimensional results establish the robustness of the proposed framework and demonstrate its applicability to a broader class of elliptic partial differential equations.

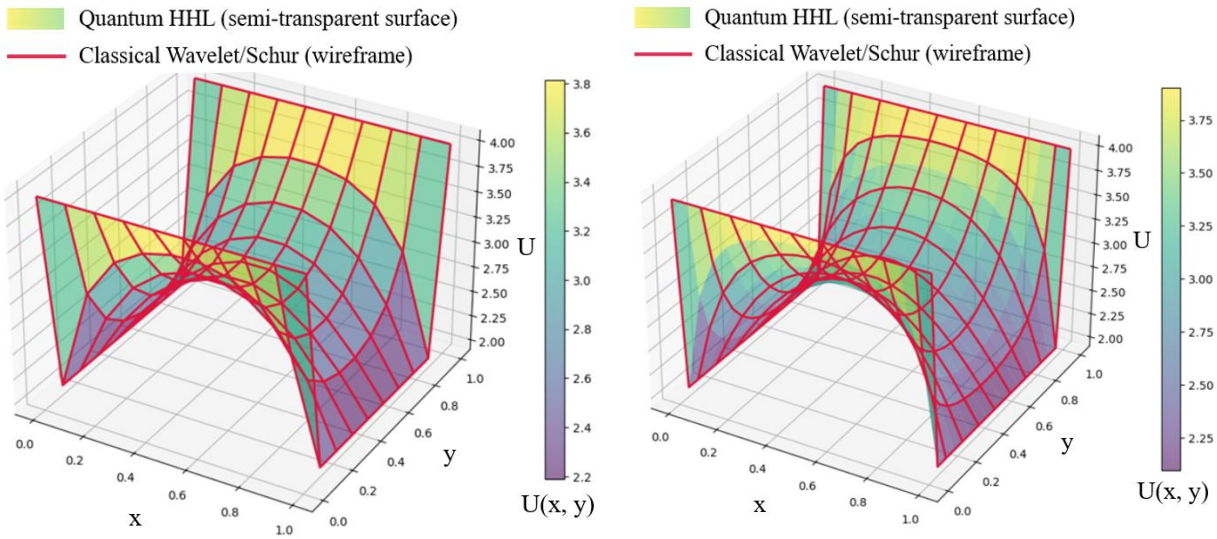


(a) Measurement Statistics (b) Recovered Solution Amplitudes

Fig. 4 Representative HHL simulation diagnostics for the two-dimensional Laplace benchmark. (a) Computational-basis measurement counts obtained from 4,096 simulated shots. (b) Real amplitudes extracted from the noiseless statevector following selection of the ancilla-success and zero-phase-register subspace. These diagnostics illustrate the simulated quantum inversion stage but do not constitute a finite-shot reconstruction of the numerical solution.

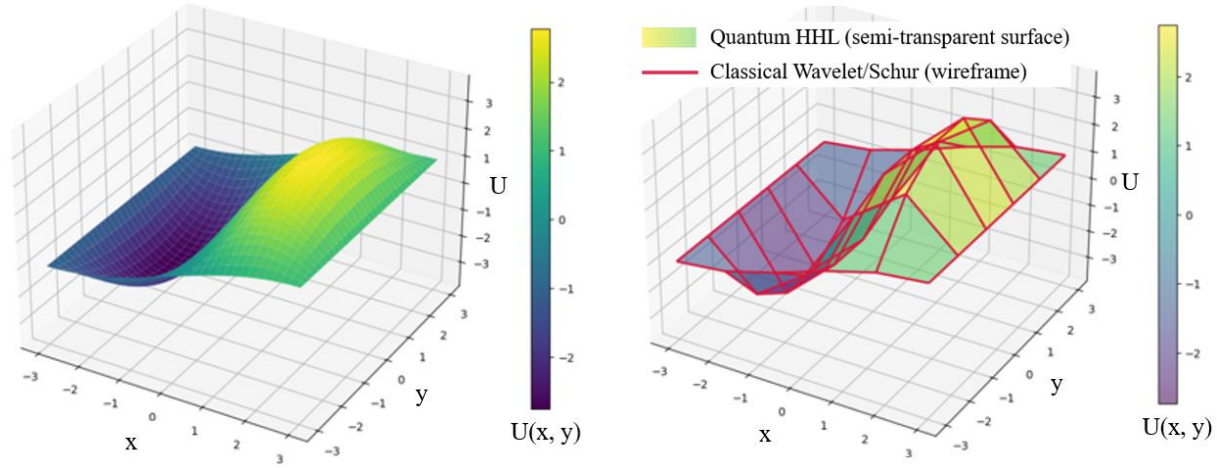


(a) Exact (b) Scale Level 2

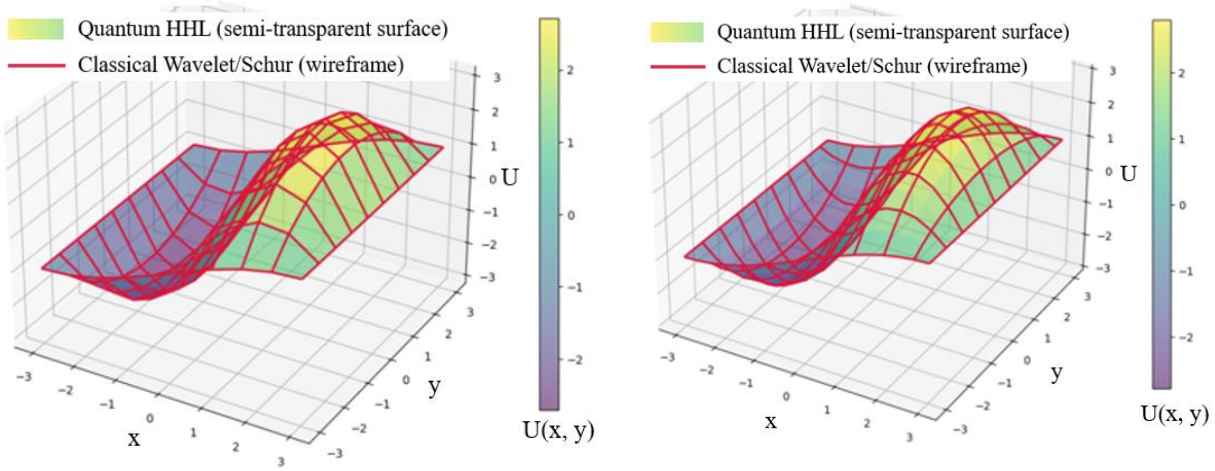


(c) Scale Level 3 (d) Scale Level 4

Fig. 5 Multiresolution reconstructions for the two-dimensional Laplace problem (Eq. 40). Panel (a) shows the high-resolution finite-difference reference solution $U(x, y)$, while panels (b)–(d) present the corresponding reconstructions at multiresolution levels 2–4. In each reconstructed panel, the semi-transparent surface represents the hybrid HHL–Wavelet–Schur solution and the red wireframe denotes the classical wavelet–Schur reconstruction. Both approaches converge systematically toward the reference solution as the multiresolution level increases, with the hybrid reconstruction closely reproducing the classical Schur solution throughout the refinement process.



(a) Exact (b)Scale level 2



(c) Scale level 3 (d) Scale level 4

Fig. 6 Multiresolution reconstructions for the two-dimensional Helmholtz-type problem (Eq. 41). Panel (a) shows the high-resolution finite-difference reference solution $U(x, y)$, while panels (b)–(d) present the corresponding reconstructions at multiresolution levels 2–4. In each reconstructed panel, the semi-transparent surface represents the hybrid HHL–Wavelet–Schur solution and the red wireframe denotes the classical wavelet–Schur reconstruction. As the multiresolution level increases, both reconstructions progressively recover the oscillatory interior structure of the reference solution, with the hybrid reconstruction remaining in close agreement with the classical Schur solution throughout the refinement process.

3.3. Hyperbolic Benchmark Problems

The proposed Wavelet–Schur–HHL framework was next evaluated for transient hyperbolic partial differential equations to investigate its performance for time-dependent transport and wave propagation. Two representative benchmark problems were considered: the one-dimensional linear advection equation and the two-dimensional wave equation. Unlike the elliptic benchmarks, these problems emphasize the ability of the hybrid methodology to preserve phase, amplitude, and transient solution structure while repeatedly applying the Schur reduction and quantum inversion throughout the time integration. In each case, the governing equations were discretized using second-order finite-difference schemes, after which the resulting multiresolution systems were constructed using Haar scaling and wavelet functions. The resulting wavelet-transformed systems were partitioned into coarse-scale scaling and fine-scale wavelet-detail components. Schur-complement reduction was then used to construct a lower-dimensional system for quantum inversion, followed by classical recovery of the eliminated coefficients and reconstruction of the complete multiresolution solution.

High-resolution finite-difference solutions were computed throughout and serve as the reference solutions for all comparisons.

The first hyperbolic benchmark considers the one-dimensional linear advection equation,

$$\frac{\partial U(x,t)}{\partial t} + V\frac{\partial U(x,t)}{\partial x} = 0, \qquad x \in [0,100], \qquad t \geq 0, \tag{42}$$

with the initial condition

$$U(x,0) = \exp\left[-0.01(x-45)^2\right], \quad 20 \le x \le 70.$$

As in the elliptic examples, the correctness of the quantum inversion stage was first examined independently of the reconstructed solution fields. Figure 7 presents representative HHL diagnostics for the Schur-reduced advection operator. Figure 7(a) shows the measurement statistics for the computational basis states having the largest probabilities following quantum phase estimation and reciprocal-eigenvalue encoding. Although the complete quantum register is substantially larger than in the previous benchmark problems, the probability remains concentrated within the dominant computational basis states, indicating that the dominant spectral information of the reduced Schur system is efficiently represented within the quantum circuit. Figure 7(b) presents the corresponding post-selected real amplitudes of the recovered quantum solution state. The smooth distribution of the dominant amplitudes demonstrates that the HHL inversion produces a stable approximation of the reduced Schur solution suitable for subsequent classical reconstruction. Together, these diagnostics verify the expected operation of the quantum inversion stage for the transient advection problem.

The resulting numerical reconstructions are presented in Figure 8. Figures 8(a) and 8(b) compare the finite-difference reference solution with the corresponding classical wavelet–Schur and hybrid HHL reconstructions at $t = 3$s for transport velocities of $V = 2$ m/s and $V = 4$ m/s, respectively. At coarse multiresolution levels, both approaches capture the overall translation of the Gaussian pulse while exhibiting the expected loss of fine-scale resolution associated with aggressive wavelet compression. As the multiresolution level increases, both reconstructions progressively recover the reference solution, with the hybrid reconstruction remaining in close agreement with the classical wavelet–Schur solution throughout the refinement process. Figures 8(c) and 8(d) illustrate the temporal evolution of the transported pulse at $t = 0$, 3, and 6s for both transport speeds. The hybrid reconstruction accurately preserves the propagation speed, pulse location, and overall waveform during the transient evolution, while maintaining close agreement with the corresponding classical multiresolution solution. The pulse remains well localized throughout the simulation, indicating that the combined wavelet–Schur reduction and HHL inversion preserve the principal transport characteristics of the underlying advection equation.

A separate quantitative validation was performed for the one-dimensional advection problem using a transport velocity of V = 8 m/s, a spatial discretization of 64 degrees of freedom, and a time increment of $\Delta t = 0.5$ s. A single-level orthonormal Haar decomposition reduced the original system to a 32-dimensional Schur-complement problem. Because the resulting Schur operator is nonsymmetric, the Hermitian block embedding described in Section 2.2 was used for the HHL inversion. The relative Frobenius norm of the skew-symmetric component was 0.3637, while the condition number of the Schur operator was 2.5752. Direct

classical solution of the Hermitian-embedded system reproduced the original Schur solution to machine precision, confirming the algebraic equivalence of the two formulations.

The classical and hybrid coarse-scale solutions were reconstructed on the original 64-point spatial grid by recovering the eliminated Haar detail coefficients and applying the inverse orthonormal Haar transformation. The time-discrete right-hand sides were aligned with the corresponding physical times, eliminating an additional time-step offset in the reconstruction. At t = 0, 3, and 6 s, the relative L2 differences between the classical Schur reconstructions and the finite-difference solutions were 2.31×10^{-16}, 3.02×10^{-16}, and 2.45×10^{-16}, respectively. The corresponding differences between the hybrid HHL reconstructions and the finite-difference solutions were 5.09×10^{-3}, 3.24×10^{-3}, and 4.70×10^{-3}. The relative residuals of the original nonsymmetric Schur systems remained below 5.2×10^{-3} across all three time cases. These results demonstrate close agreement between the calibrated hybrid inversion and the classical discrete solution following complete physical-field reconstruction.

The distinction between hybrid inversion error and underlying discretization error is particularly important for this transport problem. The finite-difference solutions exhibited relative L2 differences of 0, 0.1353, and 0.3044 with respect to the analytical advection solution at t = 0, 3, and 6 s, respectively. The corresponding hybrid reconstruction errors relative to the analytical solution were 0.00509, 0.1350, and 0.3043. Thus, the principal source of disagreement with the analytical solution at later times is the finite-difference discretization rather than the additional HHL approximation. These results were obtained using noiseless statevector simulation, with the global HHL solution amplitude calibrated against the classical Schur coefficient vector. Accordingly, the reported hybrid errors characterize calibrated numerical agreement and do not constitute an independent finite-shot or hardware-level accuracy assessment.

Table 2. Quantitative validation of the one-dimensional advection benchmark at V=8 m/s and N=64.

Relative L_2 error	t=0 s	t=3 s	t=6 s
Classical Schur vs. FD	2.31×10^{-16}	3.02×10^{-16}	2.45×10^{-16}
Hybrid HHL vs. FD	5.09×10^{-3}	3.24×10^{-3}	4.70×10^{-3}
FD vs. analytical	0	0.1353	0.3044
Hybrid HHL vs. analytical	5.09×10^{-3}	0.1350	0.3043
Hybrid coarse coefficients vs. classical	5.09×10^{-3}	3.24×10^{-3}	4.75×10^{-3}

Note: FD denotes finite difference. Hybrid HHL results were obtained using noiseless statevector simulation and classical-reference amplitude calibration.

To further evaluate the methodology for multidimensional hyperbolic systems, the framework was applied to the two-dimensional wave equation,

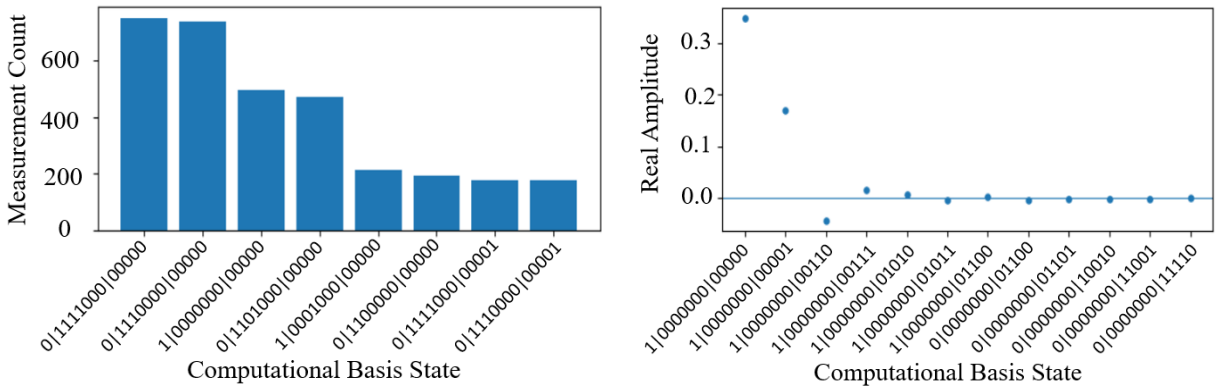
$$\frac{\partial^2 u}{\partial t^2} = c^2 \left(\frac{\partial^2 u}{\partial x^2} + \frac{\partial^2 u}{\partial y^2}\right), \qquad (x, y) \in [0,1] \times [0,1], \qquad c = 2, \tag{43}$$

with initial condition

$$u(x, y, 0) = \sin(\pi x)\sin(2\pi y),$$

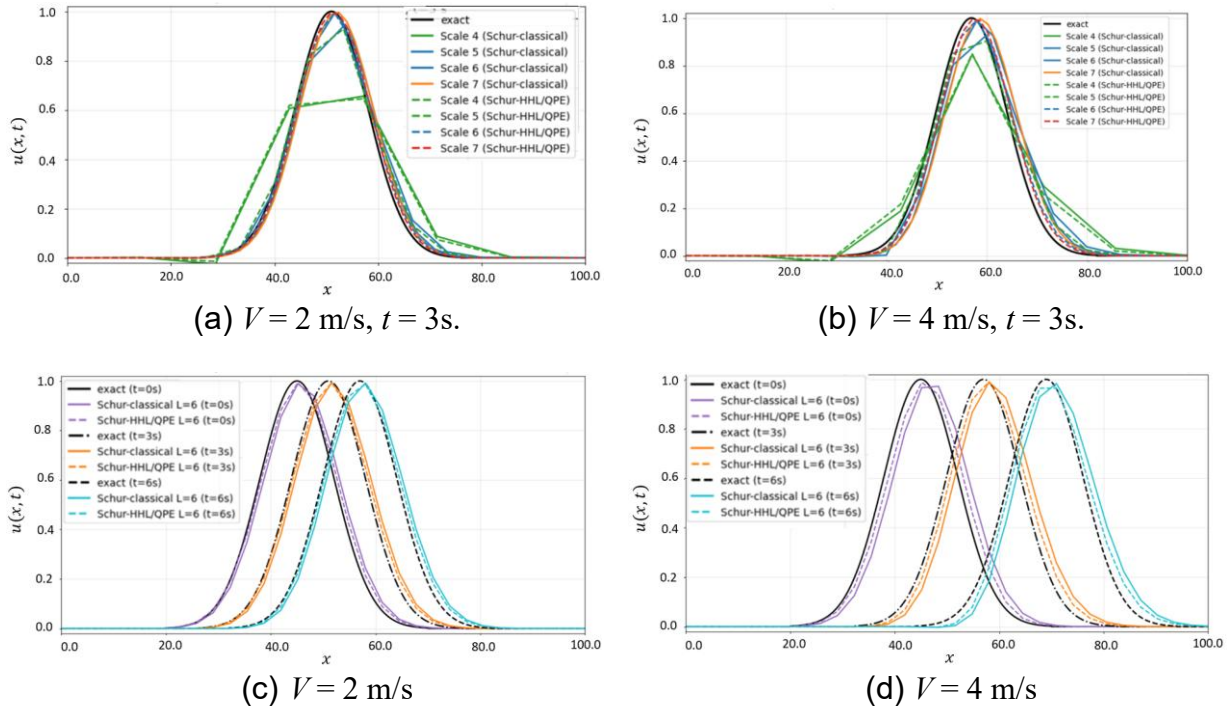
and homogeneous Dirichlet boundary conditions imposed on all domain boundaries. Representative solution fields are shown in Figure 9 for two multiresolution levels and six representative time instants spanning the first oscillation cycle. The semi-transparent surfaces denote the hybrid HHL reconstructions, while the red wireframes represent the corresponding classical wavelet–Schur solutions. At the coarser multiresolution level, the dominant standing-wave structure, nodal lines, and oscillatory behavior are accurately reproduced despite the reduced spatial representation. Increasing the multiresolution level substantially improves the representation of the wave field, with the hybrid and classical reconstructions becoming nearly indistinguishable throughout the computational domain. The close agreement between the two approaches demonstrates that the HHL inversion accurately reproduces the reduced Schur solution while preserving the transient evolution of the multidimensional wave field.

Collectively, the hyperbolic benchmark problems demonstrate that the proposed Wavelet–Schur–HHL methodology extends naturally from steady elliptic systems to transient transport and wave propagation problems. Figure 7 verifies the correct operation of the HHL inversion stage for the Schur-reduced advection operator, while Figures 8 and 9 demonstrate that the resulting hybrid reconstructions accurately reproduce the corresponding classical wavelet–Schur solutions throughout the transient evolution. Across both one- and two-dimensional hyperbolic benchmarks, the hybrid framework preserves the principal phase, amplitude, and propagation characteristics of the reference solutions while maintaining the multiresolution efficiency of the underlying wavelet–Schur formulation. These results further demonstrate the robustness and generality of the proposed hybrid methodology across a broad class of linear time-dependent partial differential equations.



(a) Counts (b) Real Amplitude

Fig. 7 Representative HHL simulation diagnostics for the one-dimensional advection benchmark (Eq. (42)). (a) Computational-basis measurement counts from the simulated HHL circuit. (b) Real amplitudes extracted from the postselected statevector. These results illustrate the circuit output and recovered statevector components used in the hybrid reconstruction, rather than a measurement-based estimation of the numerical solution.



(a) $V = 2$ m/s, $t = 3$s. (b) $V = 4$ m/s, $t = 3$s.

(c) $V = 2$ m/s (d) $V = 4$ m/s

Fig. 8 Multiresolution reconstructions for the one-dimensional advection equation (Eq. 42). Panels (a) and (b) compare the finite-difference reference solution with the corresponding classical wavelet–Schur and hybrid HHL–Wavelet–Schur reconstructions at $t = 3$s for transport velocities of $V = 2$m/s and $V = 4$m/s, respectively. Panels (c) and (d) illustrate the temporal evolution of the transported pulse at $t = 0$, 3, and 6 s for both transport speeds. Across all multiresolution levels, the hybrid and classical reconstructions preserve the principal translation and shape of the pulse while progressively approaching the finite-difference reference as the multiresolution level increases. The close agreement between the hybrid and classical reconstructions demonstrates that the proposed Wavelet–Schur–HHL methodology accurately reproduces the transient transport behavior of the advection equation.

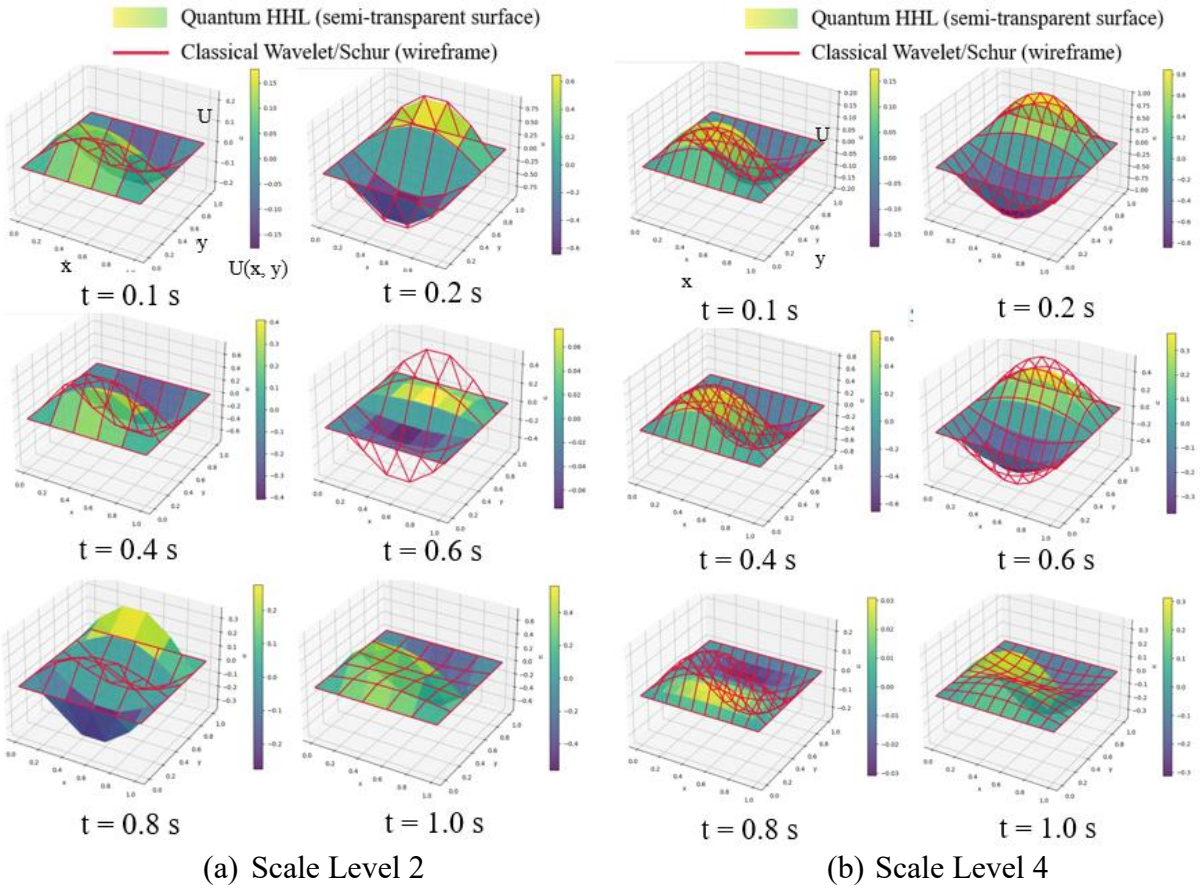


Fig. 9 Time-evolving multiresolution reconstructions for the two-dimensional wave equation (Eq. 43). Panel (a) presents the hybrid HHL–Wavelet–Schur and classical wavelet–Schur solutions at multiresolution level 2, while panel (b) shows the corresponding reconstructions at multiresolution level 4. Each panel contains representative solution fields at $t = 0.1$, 0.2, 0.4, 0.6, 0.8, and 1.0 s. In every snapshot, the semi-transparent surface represents the hybrid HHL–Wavelet–Schur reconstruction and the red wireframe denotes the classical wavelet–Schur solution. As the multiresolution level increases, both reconstructions preserve the evolving wave structure with increasing fidelity, while the hybrid reconstruction remains in close agreement with the corresponding classical wavelet–Schur solution throughout the transient evolution.

4. Conclusions

This work presented a hybrid Wavelet–Schur–HHL framework for the numerical solution of linear partial differential equations using multiresolution wavelet discretization and quantum-assisted solution of reduced linear systems. Haar-based multiresolution analysis was combined with Schur complement reduction to construct compact Schur-reduced systems suitable for quantum inversion using the Harrow–Hassidim–Lloyd (HHL) algorithm. The resulting hybrid methodology was applied to representative one- and two-dimensional elliptic and hyperbolic benchmark problems, including Poisson, oscillatory, exponential-source, Laplace, Helmholtz-type, advection, and wave equations. Throughout the study, high-resolution finite-difference

solutions served as reference solutions for evaluating both the classical wavelet–Schur formulation and the proposed hybrid approach.

The numerical experiments demonstrate several consistent observations. First, the wavelet–Schur multiresolution formulation provides an effective hierarchical representation for a broad class of linear PDEs while simultaneously reducing the size of the linear systems presented to the quantum solver. Across the one-dimensional elliptic benchmark problems, the Schur reduction consistently produced a condensed system whose condition number was approximately one-half that of the original discretized operator. Second, the hybrid HHL–Wavelet–Schur reconstructions remained in close agreement with the corresponding classical wavelet–Schur solutions for all benchmark classes considered. This agreement was observed for steady elliptic problems, multidimensional elliptic operators, transient transport equations, and time-dependent wave propagation, demonstrating that the proposed computational framework is largely independent of PDE class while preserving the convergence characteristics of the underlying multiresolution discretization.

The one-dimensional advection benchmark further demonstrated the importance of preserving nonsymmetric transport operators during quantum inversion. Using a Hermitian block embedding, the hybrid formulation reproduced the original nonsymmetric Schur system without replacing it by its symmetric part. For a 64-degree-of-freedom discretization reduced to 32 coarse-scale unknowns, the classical Haar–Schur reconstruction agreed with the finite-difference solution to machine precision, while the calibrated hybrid HHL reconstruction exhibited relative L2 differences between 0.32% and 0.51% across the three evaluated time cases. Comparison with the analytical solution also distinguished the relatively small additional hybrid inversion error from the substantially larger accumulated finite-difference discretization error. These findings support the numerical consistency of the proposed reduction, quantum inversion, and reconstruction procedure for nonsymmetric transient transport systems, subject to the stated noiseless simulation and amplitude-calibration assumptions.

The representative HHL diagnostics presented throughout the paper further verified the operation of the quantum inversion stage for both elliptic and hyperbolic systems. In each case, the measurement probabilities remained concentrated within the dominant computational basis states, and the recovered post-selected amplitudes produced stable approximations of the reduced Schur solutions suitable for classical reconstruction. Together with the numerical benchmark results, these observations demonstrate that the HHL algorithm can be successfully integrated within a multiresolution wavelet–Schur framework without disrupting the accuracy or convergence behavior of the underlying classical formulation.

The present work establishes the computational foundation for a broader program of quantum multiresolution PDE solvers. Future work will focus on developing more advanced quantum linear-system solvers that improve numerical robustness, reduce circuit complexity, and overcome several practical limitations associated with quantum phase estimation. The same multiresolution Wavelet–Schur framework will also be extended to nonlinear partial differential

equations, providing a unified hybrid quantum–classical methodology for increasingly complex multiscale problems.

While the numerical results demonstrate the feasibility of the proposed hybrid formulation and its ability to reproduce classical benchmark solutions, a rigorous assessment of computational advantage will require explicit accounting of classical preprocessing, quantum circuit resources, postselection overhead, solution recovery, and iterative refinement, together with comparisons against optimized classical solvers.

Statements and Declarations

Funding

This research was supported by the U.S. Army Engineer Research and Development Center (ERDC) through the Military Engineering Basic Research Program.

Competing Interests

The author declares that there are no financial or non-financial competing interests relevant to the content of this manuscript.

Author Contributions

J.B. Allen conceived and developed the hybrid Wavelet–Schur–HHL computational framework, performed the numerical simulations, analyzed the results, and prepared the manuscript.

Data and Code Availability

The numerical data supporting the figures and tables, simulation codes, quantum-circuit definitions, and post-processing scripts used to generate the results presented in this study, including Jupyter notebooks for the one- and two-dimensional elliptic and hyperbolic benchmark problems, are available from the corresponding author upon reasonable request.

Ethics Approval

Not applicable. This study did not involve human participants or animals.

Consent to Participate

Not applicable.

Consent for Publication

Not applicable.

References

1. LeVeque, R.J.: *Finite Difference Methods for Ordinary and Partial Differential Equations: Steady-State and Time-Dependent Problems*. Society for Industrial and Applied Mathematics, Philadelphia (2007). https://doi.org/10.1137/1.9780898717839

2. Evans, L.C.: *Partial Differential Equations*, 2nd edn. American Mathematical Society, Providence (2010). https://doi.org/10.1090/gsm/019
3. Daubechies, I.: *Ten Lectures on Wavelets*. Society for Industrial and Applied Mathematics, Philadelphia (1992). https://doi.org/10.1137/1.9781611970104
4. Mallat, S.G.: A theory for multiresolution signal decomposition: the wavelet representation. IEEE Trans. Pattern Anal. Mach. Intell. **11**(7), 674–693 (1989). https://doi.org/10.1109/34.192463
5. Meyer, Y.: *Wavelets and Operators*. Cambridge University Press, Cambridge (1995).
6. Strang, G., Nguyen, T.: *Wavelets and Filter Banks*. Wellesley-Cambridge Press, Wellesley (1996).
7. Beylkin, G., Coifman, R., Rokhlin, V.: Fast wavelet transforms and numerical algorithms I. Commun. Pure Appl. Math. **44**(2), 141–183 (1991). https://doi.org/10.1002/cpa.3160440202
8. Vasilyev, O.V., Bowman, C.: Second-generation wavelet collocation method for the solution of partial differential equations. J. Comput. Phys. **165**(2), 660–693 (2000). https://doi.org/10.1006/jcph.2000.6638
9. Allen, J.B.: Multiscale simulations of parabolic, elliptic and hyperbolic, linear PDE's using wavelet-based multiresolution analysis. Evol. Mech. Eng. **5**(5), EME.000621 (2024). https://doi.org/10.31031/EME.2024.05.000621
10. Zhang, F. (ed.): *The Schur Complement and Its Applications*. Springer, New York (2005). https://doi.org/10.1007/b105056
11. Golub, G.H., Van Loan, C.F.: *Matrix Computations*, 4th edn. Johns Hopkins University Press, Baltimore (2013).
12. Benzi, M., Golub, G.H., Liesen, J.: Numerical solution of saddle point problems. Acta Numer. **14**, 1–137 (2005). https://doi.org/10.1017/S0962492904000212
13. Harrow, A.W., Hassidim, A., Lloyd, S.: Quantum algorithm for linear systems of equations. Phys. Rev. Lett. **103**, 150502 (2009). https://doi.org/10.1103/PhysRevLett.103.150502
14. Childs, A.M., Kothari, R., Somma, R.D.: Quantum algorithm for systems of linear equations with exponentially improved dependence on precision. SIAM J. Comput. **46**(6), 1920–1950 (2017). https://doi.org/10.1137/16M1087072
15. Berry, D.W., Childs, A.M., Ostrander, A., Wang, G.: Quantum algorithm for linear differential equations with exponentially improved dependence on precision. Commun. Math. Phys. **356**, 1057–1081 (2017). https://doi.org/10.1007/s00220-017-3002-y
16. Ambainis, A.: Variable time amplitude amplification and quantum algorithms for linear algebra problems. In: 29th International Symposium on Theoretical Aspects of Computer Science (STACS 2012), Leibniz International Proceedings in Informatics, vol. 14, pp. 636–647 (2012). https://doi.org/10.4230/LIPIcs.STACS.2012.636
17. Childs, A.M., Wiebe, N.: Hamiltonian simulation using linear combinations of unitary operations. Quantum Inf. Comput. **12**(11–12), 901–924 (2012). https://doi.org/10.26421/QIC12.11-12-1

18. Costa, P.C.S., Jordan, S.P., Ostrander, A.: Quantum algorithm for simulating the wave equation. Phys. Rev. A **99**, 012323 (2019). https://doi.org/10.1103/PhysRevA.99.012323
19. Jordan, S.P., Lee, K.S.M., Preskill, J.: Quantum algorithms for quantum field theories. Science **336**(6085), 1130–1133 (2012). https://doi.org/10.1126/science.1217069
20. Montanaro, A.: Quantum algorithms: an overview. npj Quantum Inf. **2**, 15023 (2016). https://doi.org/10.1038/npjqi.2015.23
21. Nielsen, M.A., Chuang, I.L.: *Quantum Computation and Quantum Information*, 10th anniversary edn. Cambridge University Press, Cambridge (2010).